Check for updates

Non-invasive cellular-resolution retinal imaging with two-photon excited fluorescence

DANIEL J. WAHL,[1,*] **MYEONG JIN JU,**[1] **YIFAN JIAN,**[1,2] **AND MARINKO V. SARUNIC**[1]

[1]*Engineering Science, Simon Fraser University, Burnaby, BC, Canada*
[2]*Casey Eye Institute, Oregon Health & Science University, Portland, OR 97239, USA*
[*]dwahl@sfu.ca

Abstract: Two-photon excited fluorescence (TPEF) imaging of the retina is a developing technique that provides non-invasive compound-specific measurements from the retina. In this report, we demonstrate high-resolution TPEF imaging of the mouse retina using sensorless adaptive optics (SAO) and optical coherence tomography (OCT). A single near-infrared light source was used for simultaneous multi-modal imaging with OCT and TPEF. The image-based SAO could be performed using the *en face* OCT or the TPEF for aberration correction. Our results demonstrate OCT and TPEF for angiography. Also, we demonstrate non-invasive cellular-resolution imaging of fluorescently labelled cells and the Retinal Pigment Epithelium (RPE) mosaic.

1. Introduction

Non-invasive retinal imaging is a valuable tool that is used in both clinical and preclinical vision research to aid the development of novel therapies for preventing irreversible vision loss. More sensitive assessment of the physiological and biochemical processes within the retina could be used to detect earlier signs of disease in order to preserve sight [1,2]. Fluorescence can be used to image many biomarkers, since fluorophores can be added to the retina to provide contrast or fluorophores that are intrinsic to the retina can be used for measurements. For example, measuring autofluorescence from the Retinal Pigment Epithelium (RPE) is of high interest for investigating diseases such as Age-Related Macular Degeneration (AMD) and Stargardt disease [3–5].

For many fluorophores intrinsic to the retina, the single-photon excitation is in the ultraviolet (UV) range and the fluorescence cannot be excited through the eye of many species due to the ocular transmission window [6,7]. Imaging the retina non-invasively with Two-Photon Excited Fluorescence (TPEF) could enable novel *in vivo* studies of disease and retinal physiology [6–9]. Furthermore, the multiphoton process suppresses out-of-focus background signal, which improves the axial sectioning without a confocal aperture in the optical detection path. Imaging the retina with near-infrared (NIR) light has advantages since the retina is less sensitive to NIR than visible light. NIR light is also less scattered within biological tissue than the equivalent visible light required to excite the same fluorophores [10,11].

The difficulty of retinal TPEF imaging *in vivo* is that high energy is typically required to generate the TPEF, while minimizing the incident exposure energy is required for the imaging to be non-invasive. An active area of research is the development of technology that reduces the average laser power required for TPEF imaging in the eye [1,5,12]. The TPEF signal intensity is highly sensitive to the focused spot size, which leads to high sensitivity to aberrations [11]. It has been demonstrated that the TPEF signal for retinal imaging can be increased by using Adaptive Optics (AO) for aberration correction [8,12,13].

For high-resolution imaging of the mouse retina, optical aberrations introduced by the eye must be corrected for diffraction-limited imaging. AO has been demonstrated to correct ocular

aberrations extensively [3,14–16]. The traditional approach to AO is to use a Wavefront Sensor (WFS) to directly measure the aberrations. Alternatively, it has also been demonstrated that Sensorless AO (SAO) can provide depth-resolved aberration correction using an image-based approach. SAO has the advantage of avoiding the system complexities that are required due to the short length of the mouse eye, which creates an optically thick sample with multiple scattering surfaces [17].

In this paper, we present a multi-modal imaging system that uses SAO and Optical Coherence Tomography (OCT) to achieve non-invasive TPEF imaging of cellular features in the retina. We used the same light source to simultaneously generate OCT and TPEF, where both imaging modalities could be used to drive the SAO optimization algorithm. We demonstrate the high-resolution OCT/TPEF system with a variety of samples, which included Fluorescein Angiography (FA) and fluorescently labelled cells. We also demonstrate the ability to non-invasively image intrinsic fluorescence from the RPE of the mouse retina in various strains.

2. Methods

2.1. System setup

The SAO OCT TPEF imaging system used a femtosecond pulsed laser (Mai Tai HP, Spectra-Physics, CA, USA) for both the OCT and TPEF excitation. The laser had a tuning range from 690 nm to 1040 nm, where the central wavelength was chosen for each of the sample fluorophores. Table 1 summarizes the calculations to estimate the axial resolution of the OCT in tissue [18] and the maximum laser power used for each fluorophore imaged in this report. The laser power could be adjusted with neutral density filters. A schematic of the imaging system is presented in Fig. 1.
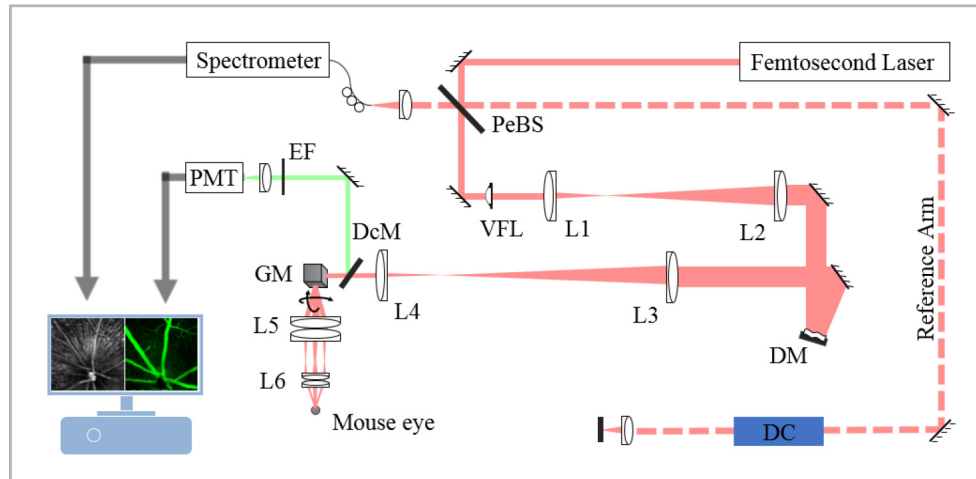
Fig. 1. Schematic of the Sensorless Adaptive Optics (SAO) Optical Coherence Tomography (OCT) and Two-Photon Excitation Fluorescence (TPEF) imaging system. The imaging system was constructed with a pellicle beam splitter (PeBS), a variable focus lens (VFL), a deformable mirror (DM), a dichroic mirror (DcM), galvanometer-scanning mirrors (GM), emission filters (EF), a photo-multiplier tube (PMT), dispersion compensation (DC), and the following lenses: L1 = 100 mm, L2 = 300 mm, L3 = 400 mm, L4 = 100 mm, L5 = 2×125 mm, L6 = 2×50 mm. The reference arm denoted as a dashed line.

For the OCT/TPEF system, we used a pellicle beam splitter to separate the light into the sample arm and the reference arm. In the sample arm, we used a variable focus lens (VFL, A-39N1, Corning, NY, USA) to control the focal plane within the sample, a continuous membrane deformable mirror (DM, DM-69, ALPAO, France) to correct the wavefront aberrations, and XY

Table 1. Laser specifications used for each fluorescent sample and the calculated resolution.

Fluorescent Sample	Center Wavelength (nm)	Spectral Bandwidth (nm)	Laser Power (mW)	Lateral Spot Size (μm)	TPEF Axial Resolution (μm)	OCT Axial Resolution (μm)
FA	800	13	< 3	2.0	29	16
GFP	910	16	< 9	2.2	33	17
YFP	940	15	< 3	2.3	34	19
RPE	740	8.2	< 8	1.8	26	22

mounted pair of galvanometer-scanning mirrors (GM, 6215H, Cambridge Technology Inc., MA, USA) to scan the light across the sample. The scanning angles of the GMs could be adjusted to change the imaging field of view (FOV) on the retina and the maximum FOV for this system was ~25 degrees (~850 μm). Three lens-based telescopes were used to optically relay the pupil planes at the VFL, DM, and GMs to the mouse eye. The telescopes were constructed with achromatic doublets that had focal lengths listed in Fig. 1. The imaging beam entered the mouse eye with an NA of ~0.25. Table 1 summarizes the calculations to estimate the spot size in tissue using the Airy disk radius and the FWHM of the axial point spread function for each center wavelength [19]. The reference arm included dispersion compensating glass to match the sample arm.

For OCT, back-scattered light from the eye and the light returning from the reference arm were combined at the PeBS and coupled into a single mode fiber. The spectral interference signal was then detected by a custom-built spectrometer (1024 pixels, 100 kHz, Bioptigen Inc., NC, USA) with a spectral range from ~730 nm to ~995 nm. The data was acquired through a Camera Link frame grabber board (PCIe-1433, National Instrument, Austin, TX) and processed using a custom GPU-accelerated program for real-time processing and display [20]. The two-dimensional transverse area (*en face*) was scanned and sampled with 400×200 A-scans, which resulted in an acquisition rate of 1 volume per second. For OCT-based Angiography (OCTA), we used two intensity B-scans (two BM-scans) to calculate the angiography at 400×200 (200×2) A-scans. During the SAO-OCT optimization process, the density in the direction of the slow scan was reduced to 400×20 A-scans for aberration correction using the *en face* OCT images.

TPEF emission from the sample was de-scanned by the GMs and reflected by the dichroic mirror (DcM) to the photo-multiplier tube (PMT, H7422P-40, Hamamatsu Photonics, Japan) detector. The short-pass filters (FF01-650/SP-25, FF01-720/SP-25, IDEX Health & Science LLC, NY, USA), a lens, and an aperture were positioned before the PMT to reject stray light. The electric current from the PMT was converted to a voltage with a transimpedance amplifier (LCA-400K-10M, FEMTO Messtechnik GmbH, Germany) and digitized by a DAQ device (PCIe-6361, National Instrument, TX, USA). The digitization of the PMT signal was synchronized with the OCT A-scans for simultaneous operations, which ensured that both OCT and TPEF images were co-registered. The TPEF could also be operated without the OCT to acquire at 10 frames per second for averaging in post-processing.

The SAO optimization used a hill-climbing coordinate-search algorithm, which was recently reported for mouse retinal imaging [21][22]. In brief, the optimization used the merit function defined by the image sharpness of the *en face* OCT images that were extracted at the user-selected depth or the TPEF images. The algorithm began by finding the best initial defocus value, then the astigmatisms, and then continuing in ascending order for a total of 18 modes. Multiple iterations could be performed to ensure optimal the aberration correction. The optimization required ~20 seconds per iteration using either the OCT or the TPEF images.

2.2. Animal handling and image processing

The mouse imaging was performed under protocols compliant to the Canadian Council on Animal Care and the approval of the University Animal Care Committee at Simon Fraser University. A subcutaneous injection of ketamine (100 mg/kg of body weight) and dexmedetomidine (0.1 mg/kg of body weight) was used to anesthetize the mouse prior to imaging. The pupils of the mouse were dilated with a drop of topical solution (Tropicamide, 1%). A rigid 0-Diopter contact lens was placed on the mouse eyes to prevent dehydration of the cornea. Then, the animal was aligned to the imaging system without any contact [23]. All of the mice imaged in this work were purchased from The Jackson Laboratory, ME, USA, which included B6 mice (C57BL/6J), albino B6 mice (B6(Cg)-Tyr^{c-2J}/J), mice with GFP labelled microglia (B6.129P-Cx3cr1^{tm1Litt}/J), mice with GFP labelled retinal ganglion cells (Tg(Thy1-EGFP)MJrs/J), mice with YFP labelled neural cells (B6.Cg-Tg(Thy1-YFP)16Jrs/J), and mice with a mutated rpe65 gene (B6(A)-Rpe65^{rd12}/J). Table 2 summarizes the that mice used for the imaging presented in this report. In addition, all the mice were female and weighed 25–35 grams. For fluorescence angiography, the mice were anesthetized and then subcutaneously injected with 100 μL of 100 mg/mL fluorescein.

Table 2. Summary of mice that were used in this report.

Mouse Strain	Stock Number	Pigmentation	Number
C57BL/6J	000664	Pigmented	1
B6(Cg)-Tyr{c-2J}/J	000058	Albino	3
B6.129P-Cx3cr1{tm1Litt}/J	005582	Pigmented	3
Tg(Thy1-EGFP)MJrs/J	007788	Pigmented	1
B6.Cg-Tg(Thy1-YFP)16Jrs/J	003709	Pigmented	1
B6(A)-Rpe65{rd12}/J	005379	Pigmented	2

The images in this report were generated with post-processing steps that were performed using Matlab (MathWorks Inc, MA, USA) and ImageJ (National Institutes of Health, MD, USA), which included steps to register, average, and contrast stretch the images [21]. For OCT images, we recorded 5 volumes per acquisition. For TPEF images of fluorescently labelled cells and FA, we recorded 100 frames per acquisition. For TPEF images of the RPE layer, we recorded 300 to 900 frames per acquisition. The OCT images presented in this work are either cross-sectional B-scans in the fast scanning direction, or the *en face* view at a user-selected depth. The OCT B-scans were aligned to remove axial motion with a vertical translation to maximize the cross-correlation between the images. The B-scans presented in this report were an average of 5 adjacent B-scans within one of the acquired volumes. The *en face* OCT and OCTA images were generated with a Maximum Intensity Projection (MIP) between two manually selected axial positions on the B-scans, which corresponded to the focal plane within the sample. From five *en face* OCT/OCTA volumes that were acquired sequentially, one image was selected as the template image and the other images were registered to the template image prior to averaging. In the registration process, vertical and horizontal image translations were first performed to maximize the cross-correlation between the template and moving image. Then, each image was non-rigidly aligned to the template with a sum of squared differences similarity metric along cubic B-splines using the Medical Image Registration Toolbox (MIRT) [24]. For the TPEF images, the same rigid and non-rigid steps were used to register each frame to the template. However, the unregistered average image was used as a template [12]. After registration, the OCT/OCTA and TPEF images were averaged, the image pixel intensity was scaled for presentation if required, and the images were resized to have the same vertical and horizontal scale. The images that were acquired at multiple depths from the same eye and the images before/after SAO were processed identically

for comparisons. We estimated the peak signal-to-noise ratio (SNR) defined by Eq. 1 [25,26]:

$$SNR = 10 \log \frac{\max{(I)}^2}{\sigma_b^2}, \tag{1}$$

Where I is the image pixel intensities and σ_b^2 is the variance, which was calculated from a region within the image that only contained background noise.

3.   Results

The results are split into three parts for each type of fluorophore that was imaged in the mouse eye. Please see section 3.1 for Fluorescein Angiography (FA), where we used OCT to guide the aberrations correction to reduce the laser power to < 3 mW. Section 3.2 we demonstrate the imaging performance with fluorescently labelled cells and Section 3.3 we demonstrate imaging of the RPE layer with SAO in a variety of mouse strains.

3.1.   Fluorescein angiography

The murine vasculature of the inner retina is stacked in three distinct layers, including the Outer Plexiform Layer (OPL), Inner Plexiform Layer (IPL), and Nerve Fiber Layer (NFL). This hierarchical structure provides an opportunity to demonstrate the depth-resolved aberration correction and the ability of TPEF to provide axial sectioning without a confocal aperture. In Fig. 2, the laser power was adjusted to 2.5 mW, and the focal plane was positioned at the OPL of a 6-month-old albino B6 mouse (B6(Cg)-Tyr^{c-2J}/J). Then, the SAO wavefront optimization was performed using the *en face* OCT images of the OPL, which were extracted from the B-scans between the two depth positions that are marked by yellow arrows in Fig. 2. The SAO optimization was performed with 2 iterations for a total algorithmic execution time of ~40 seconds. The top and bottom rows of Fig. 2 are before and after the aberration correction, respectively. The first column shows the improvement in the OCT B-scans (linear scale) at the OPL layer. The OCT B-scans were selected from the cross-section between the blue arrows on the *en face* OCT. The middle column shows the improvement in the sharpness and brightness in the *en face* OCT. The third column shows improvement of the TPEF images that resulted from the wavefront optimization on the *en face* OCT images. The TPEF images were estimated to have an SNR of 26.3 dB before aberration correction and 31.0 dB after OCT-guided aberration correction using Eq. 1.

   After SAO at the OPL, using the same aberration correction, OCT and OCTA volumes were acquired while shifting the focus to the OPL, IPL, and NFL using the tunable lens, as shown in Fig. 3(a). The OCT B-scans in top row were from the same location as in Fig. 2, where the shift in focal plane can be seen by the change in image intensities along the depth of the B-scan. The B-scans focused on the OPL, IPL, and NFL were color-coded in depth and composited with a Maximum Intensity Projection (MIP), as shown in Fig. 3(a) (top right). Similarly, TPEF images were acquired while shifting the focus with the tunable lens through the inner retinal layers from the OPL to the NFL to create a depth-stack (z-stack). TPEF images were acquired at 25 depth location with increments of ~5 μm through the inner retina. The bottom row of Fig. 3(a) shows the TPEF images focused at the OPL, IPL, and NFL. The TPEF images were composited with color corresponding to the relative location between the OPL and NFL (bottom right), which matched the color-coded OCT B-scan (top right). The red arrows in Fig. 3(a) point to a few connecting or diving vessels between the retinal layers [27,28], which appear clearly in the TPEF FA. However, these vessels are not clearly identifiable as connecting vessels in the OCTA.

   In order to demonstrate the effect of the SAO-OCT optimization on the TPEF imaging in a cross-sectional view, TPEF z-stacks were resliced to generate a cross-section in the same direction as the OCT B-scans (fast scan direction). Prior to the extraction of TPEF cross-sectional images
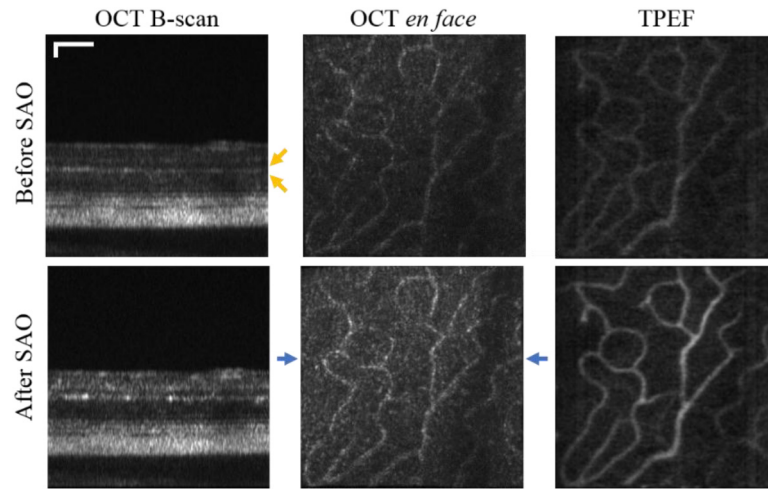
Fig. 2. Optical Coherence Tomography (OCT) and Two-Photon Excited Fluorescence (TPEF) images of the mouse retina before (top row) and after (bottom row) OCT-guided Sensorless Adaptive Optics (SAO). The improvement in the OCT B-scan is shown in the left column, the improvement in the *en face* OCT is shown in the middle column, and the improvement in the TPEF is shown in the right column. The yellow arrows represent the imaging focal position and the line between the blue arrows represents the cross-sectional location of the OCT B-scans. Scale bars: 50 μm.

from the TPEF volume, the 25 TPEF images were interpolated to 75 pixels in depth to scale with the OCT B-scans. Figure 3(b) shows the TPEF cross-sections before and after SAO optimization. The image intensity was plotted between the blue arrows and the red arrows in Fig. 3(b) to show the improvement due to the aberration correction. The TPEF cross-sectional slices presented in Fig. 3(b) had two distinctive blood vessels on top of each other, which demonstrates the axial sectioning ability of the TPEF.

3.2.   *GFP and YFP labelled cells*

GFP labelled cells have small features that can be used to demonstrate the imaging resolution of the TPEF system. In this section, we demonstrate the ability to visualize cellular features after SAO optimization.

We imaged a mouse strain with GFP labelled microglia (B6.129P2(Cg)-Cx3cr1^{tm1Litt}/J) with a center wavelength of 910 nm. Figure 4(a) shows a single TPEF image frame (left), and then an average of 100 frames (right). First, OCT B-scans were used to navigate to the focal plane where we would expect to find the GFP labelled cells. Then, as shown in Fig. 4(b), we decreased the imaging FOV to ~70 μm to performed the SAO optimization using the fluorescence images. The SAO optimization was performed with 5 iterations for a total algorithmic execution time of ~100 seconds. The example in Fig. 4(b) demonstrates an overall image improvement from an SNR of 33.6 dB before aberration correction to 36.6 dB after aberration correction using Eq. (1). There was also an improvement in the features of the microglia branches that are visualized after aberration correction. The images in Fig. 4(a) and 4(b) were from two mice that were both 18 months of age. In Fig. 4(c), we show another image after aberration correction with a FOV that was ~100 μm from another mouse that was also 18 months of age.

We also demonstrate the ability to image GFP labelled retinal ganglion cells (RGC) of a transgenic mouse strain (Tg(Thy1-EGFP)MJrs/J) with SAO-TPEF and we compared the images to single photon excited fluorescence (SPEF) with SAO. Figure 5 (left) shows an image of a RGC
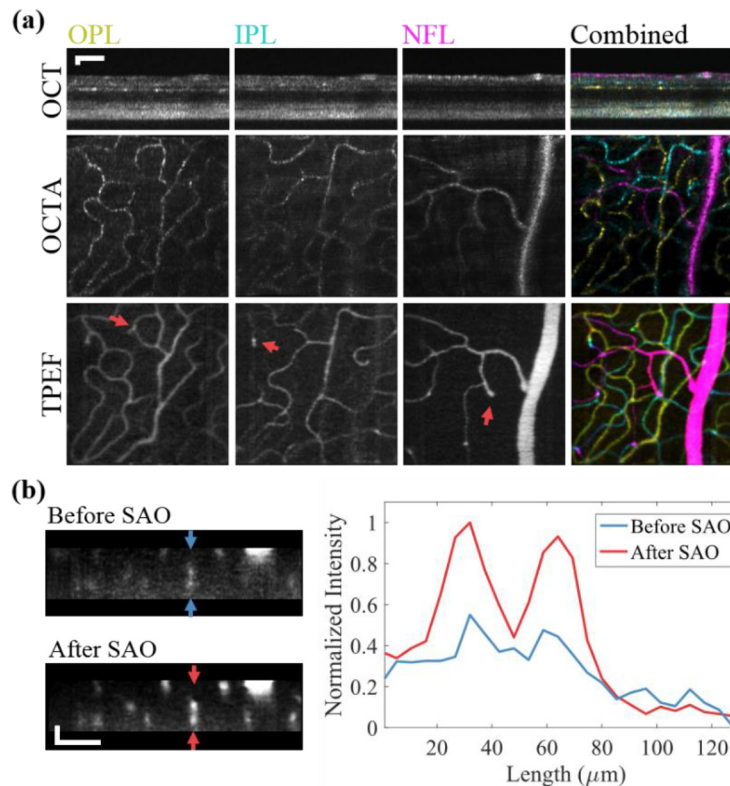
Fig. 3. (a) OCT B-scans (top row), OCTA *en face* (middle row), and TPEF (bottom row) with the focal plane at the Outer Plexiform Layer (OPL), Inner Plexiform Layer (IPL), and Nerve Fiber Layer (NFL). In the right column, the images of the vascular layers were composited with a MIP. The red arrows point out connecting vessels in the TPEF. (b) Cross-sectional TPEF images (left) of the inner retinal vasculature before and after Adaptive Optics (SAO) acquired with a 25-step z-stack that was interpolated to 75 image pixels. The axial intensity profile plot between the red and blue arrows of the TPEF cross-sectional images. Scale bars: 50 μm.

from a 14-month-old mouse after SAO-TPEF with a FOV of ~200 μm. Figure 5 (middle) shows the same cell imaged with SAO-SPEF with a matching FOV. The larger FOV of ~1.3 mm is presented in Fig. 5 (right) to show the location of the RGC relative to the optic nerve head. The imaging system used for SPEF is described in a recent report [21], which used a 488 nm laser for fluorescence excitation and the same numerical aperture (NA) into the mouse eye. By comparing these results, it appears that the TPEF imaging can resolve similar features in the lateral plane. However, the apparent size of the soma in the SPEF image is 30% larger than the soma in the TPEF image. The 'glow' of the soma is reduced in the TPEF image due to improved TPEF axial sectioning in this example.

The Thy-1 YFP-16 Line (B6.Cg-Tg(Thy1-YFP)16Jrs/J) mouse retina was also imaged using SAO-TPEF with only 2.5 mW at 940 nm . From a 7-month-old mouse, a z-stack of TPEF images were acquired throughout the inner retina to visualize the fluorescently labelled cells. In Fig. 6, the OCT B-scans on the top row are presented in linear scale to show the focal plane at the same depth location as the TPEF images in the middle row, which are focused at the NFL, IPL, and OPL.
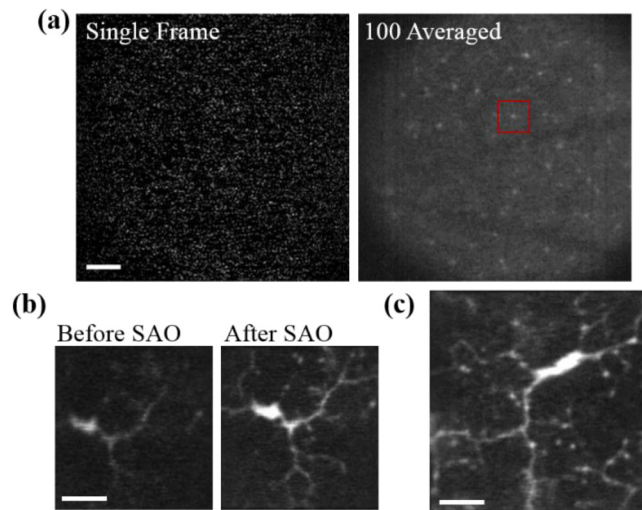
Fig. 4. TPEF imaging of GFP labelled microglia (B6.129P2(Cg)-Cx3cr1{tm1Litt}/J) in the mouse retina. (a) Single TPEF frame (left) and an average of 100 frames (right) at a ~0.8 mm FOV. The red square represents a 100 μm FOV to represent the scale of the microglia. Scale bar: 100 μm. (b) TPEF images of a GFP labelled microglia cells before (left) and after (right) Sensorless Adaptive Optics (SAO). (c) TPEF image after SAO. Scale bars: 20 μm.
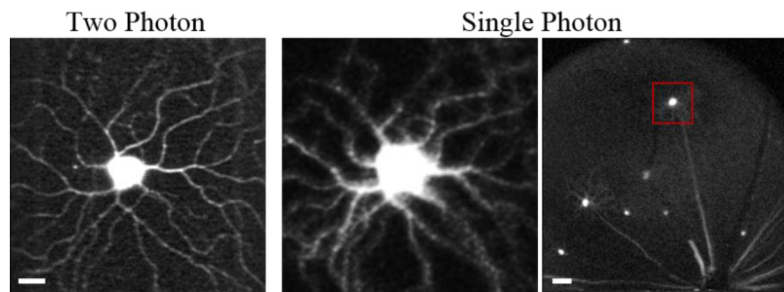

Fig. 5. Comparison of a GFP labelled retinal ganglion cell that was imaged using SAO TPEF (left) and using SAO SPEF with the same 200 μm FOV (middle). A SPEF image is also shown at a ~1.3 mm FOV (right), where the red square represents the 200 μm FOV that was used for the other images. Left scale bar: 20 μm. Right scale bar: 100 μm.

As shown by the OCT B-scans, some of the fluorescently labelled cell bodies (blue arrow) and axons (red arrow) appear to located near the NFL, whereas others cell bodies (yellow arrow) appear to be located near the OPL. The fluorescently labelled cells in the OPL could be a different type of neural cell, such as horizontal cells [29]. In the bottom row of Fig. 6, the OCTA *en face* images (magenta) were combined with the TPEF (green) with the focal plane at the NFL (left) and the OPL (right) to co-localize of the fluorescently labelled cells with the blood vessels.

3.3. RPE imaging

In the following results (Figs. 7 and 8), we demonstrate TPEF imaging of the RPE with the assistance of SAO-OCT in an albino B6 mouse (B6(Cg)-Tyr^{c-2J}/J). For Fig. 7, we imaged a mouse that was 5.5 months of age. First, the OCT was used to ensure the focal plane was at the RPE layer of the retina. In Fig. 7(a), the OCT B-scans (top row) are presented in linear scale to show the intensity change as the focal plane was shifted from the NFL (left), to the OPL (middle),
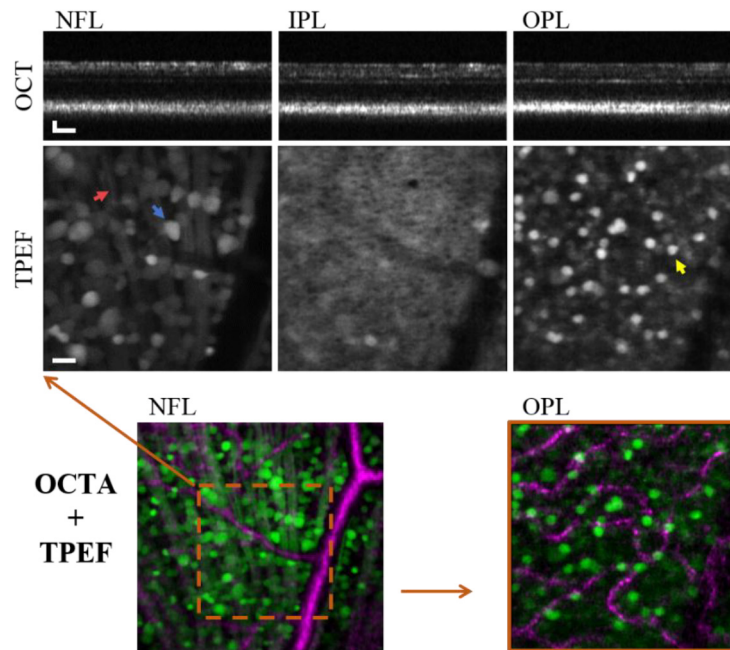
Fig. 6. OCT B-scans (top row) and TPEF (middle row) imaging with the focal plane at the Nerve Fiber Layer (NFL), Inner Plexiform Layer (IPL), and Outer Plexiform Layer (OPL) of a Thy-1 YFP-16 Line (B6.Cg-Tg(Thy1-YFP)16Jrs/J) transgenic mouse. The blue arrow and yellow arrow point at fluorescently labelled cell bodies. The red arrow points at fluorescently labelled axons. In the bottom row, the OCTA *en face* image (magenta) was composited with the TPEF image (green). Vertical scale bar: 50 μm. Horizontal scale bars: 20 μm.

and to the RPE (right). Here, we used the TPEF images to perform one iteration of the SAO optimization for a total algorithmic execution time of ~20 seconds. In Fig. 7(b) and 7(c), there was an apparent increase in signal after SAO and an improved image quality of the RPE mosaic, as shown by the line plots between the blue arrows and the red arrows. From the line plot, we can calculate a 25 - 30 μm spacing between peaks, which corresponds the spacing of the RPE cells.

We imaged the RPE of one mouse (5.5 months of age) four days apart to demonstrate the ability to perform non-invasive longitudinal imaging of the same eye over time. This interval was sufficient time for photo-chemical and photo-thermal damage to appear in the OCT [30,31]. The TPEF from the RPE and the OCT images are shown on day 1 in Fig. 8(a). The OCT B-scans are presented in log-scale and show that there was no damage immediately after using an 8 mW exposure for a few minutes. In Fig. 8(b), we imaged the same area four days later, where there was no apparent damage from the two imaging sessions. In Fig. 8(c), we have digitally zoomed into a small area of the TPEF images to show a similar RPE pattern on each day. TPEF images from day 1 (green) and day 4 (magenta) were combined with a MIP.

An advantage of working with mice is the well-established ability to manipulate their genetics. However, here, we show differences in the TPEF images from the RPE layer that resulted from a variety of mouse strains. In Fig. 9, using 740 nm excitation light, we imaged the popular pigmented B6 mouse (C57BL/6J) at 16 months of age, an albino B6 mouse (B6(Cg)-Tyr^{c-2J}/J) at 5.5 months of age, and a pigmented mouse strain with a disruption of the rpe65 gene (B6(A)-Rpe65^{rd12}/J)) at 2.5 months of age. The TPEF images from the B6 mouse had an evenly distributed signal from the RPE with only faint structures visible, as compared the albino B6 mouse, where the RPE mosaic was clear. In the pigmented rpe65 mouse, we can also visualize the RPE mosaic,
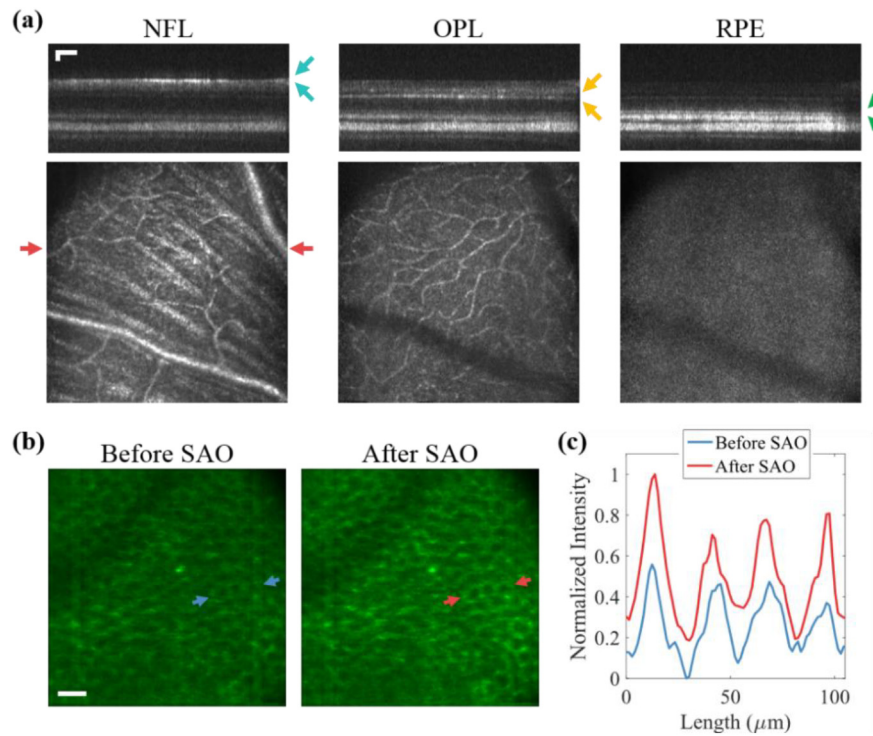
Fig. 7. (a) The SAO-OCT B-scans in linear scale (top row) and the *en face* OCT (bottom row) with the focal plane at the Nerve Fiber Layer (NFL), Outer Plexiform Layer (OPL), and Retinal Pigment Epithelium (RPE) in the mouse retina. The *en face* OCT images were extracted between the cyan arrows (NFL), yellow arrows (OPL), and green arrows (RPE). The OCT B-scans were located between the red arrows on the *en face* OCT image. (b) TPEF images of the RPE of the mouse retina before and after SAO. (c) An intensity line plot between the blue arrows and the red arrows on the TPEF images of the RPE mosaic. Scale bars: 50 μm.
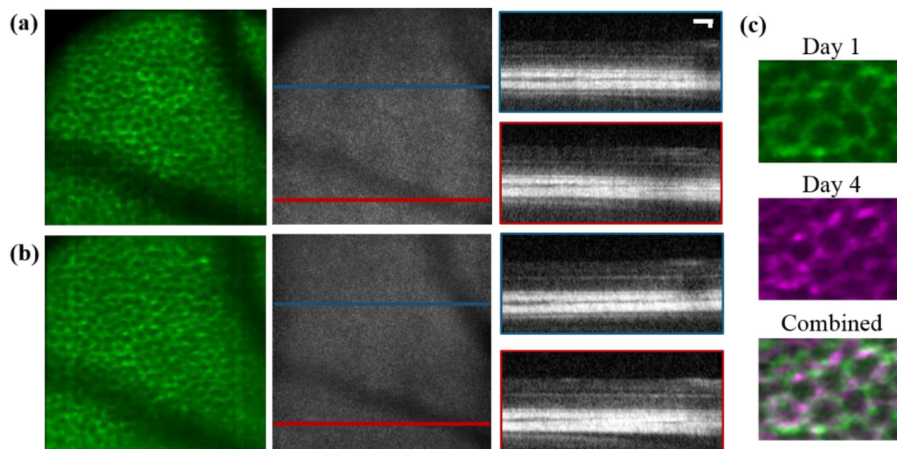

Fig. 8. (a) TPEF images of the RPE (left), *en face* OCT (middle), and OCT B-scans (right). (b) TPEF images of the RPE (left), *en face* OCT (middle), and OCT B-scans (right) from the same mouse four days later. (c) The digital enlargement of the TPEF images on day 1 (green) and day 4 (magenta), which were combined with a MIP. Scale bars: 50 μm.

which is likely due to the build-up of retinyl esters storage particles from the dysfunction in the visual system [8,9]. Fluorescent compounds in the RPE are known to accumulate with age [32], which would increase the autofluorescence in older mice and could be an additional factor that affects the visualization of the RPE mosaic.
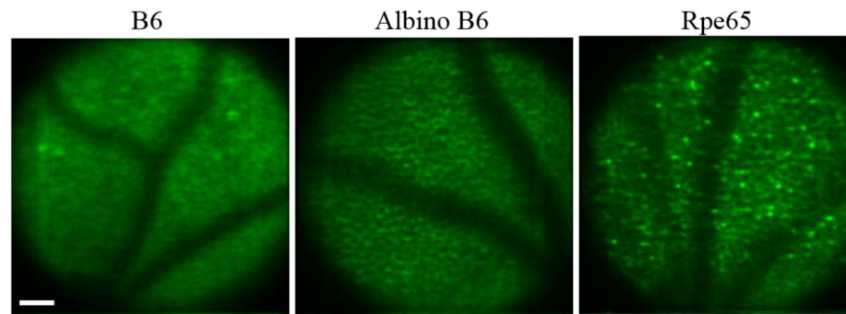
Fig. 9. TPEF from the RPE layer of the mouse retina in three different mouse strains, including a pigmented B6 mouse (C57BL/6J), an albino B6 mouse (B6(Cg)-Tyr{c-2J}/J), and a pigmented rpe65 mouse (B6(A)-Rpe65{rd12}/J). Scale bar: 100 μm.

We further investigated the ability of TPEF to provide compound-specific contrast. Figure 10 shows TPEF images at different central wavelengths from the pigmented rpe65 mouse at 18 months of age. At 760 nm, we are able to visualize the fluorophores that have accumulated near the cell membrane of the RPE cells. However, after 800 nm the TPEF signal is dominated by a more evenly distributed fluorescence signal in the RPE layer. These results agree with other Literature [6,32,33], which demonstrate that the fluorescence from the retinyl ester storage particles is more efficient at 760 nm than at longer wavelengths. At the longer wavelengths used in these results, the fluorescence emission is largely due to the compound A2E in lipofuscin. Since autofluorescent compounds, including A2E, accumulate in the RPE with age [32], there was likely more fluorescence emission with the older mouse than the rpe65 mouse imaged for Fig. 9.
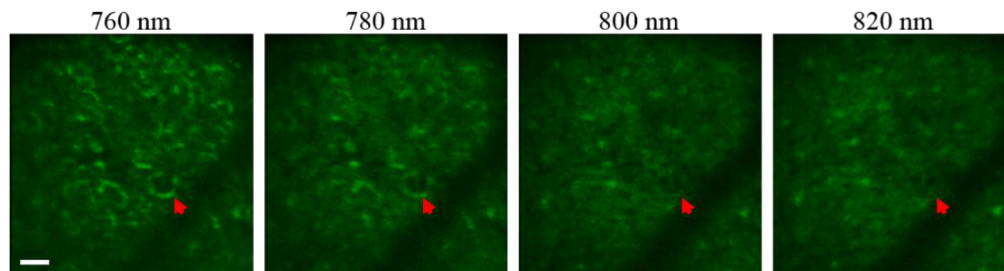
Fig. 10. TPEF image of a pigmented rpe65 mouse (B6(A)-Rpe65{rd12}/J) with different central wavelengths, including 760 nm, 780 nm, 800 nm, and 820 nm. The red arrow highlights an RPE cell where the fluorescence near the cell membrane is reduced with longer wavelengths. Scale bar: 50 μm.

4. Discussion

In this paper, we have demonstrated OCT guided TPEF imaging with image-based wavefront optimization to improve the fluorescence signal. Since the TPEF is very sensitive to the focal spot size, aberration correction is crucial for high-resolution imaging with minimal laser power. We

used a tunable femtosecond laser source to enable retinal imaging from a variety of fluorophores. The system also used a tunable lens to shift the focal plane within the retina, and a deformable mirror for aberration correction with a hill-climbing coordinate-search algorithm. Our results included high-resolution volumetric fluorescein angiography of mouse retinal vasculature, sub-cellular imaging resolution of fluorescently labelled cells, and intrinsic fluorescence imaging from the RPE. We have demonstrated that some samples can be imaged with < 3 mW of laser power, including YFP labelled cells and fluorescein angiography. We have also demonstrated RPE imaging in various mouse strains and we have shown that the amount of pigment in RPE of the particular strain can reduce the ability to visualize the RPE mosaic with TPEF.

The optical layout in this work was similar to our previously reported imaging systems for the mouse retina [34,35], which we were able to compact into a 1.5×2 ft footprint, as described in a recent report [21]. Using a similar design, the compact system would enable easier collaboration with other vision scientists.

In the mouse model, common methods such as genetic manipulation or viral injection can be used to label cells with GFP. In the Literature, TPEF imaging of GFP labelled cells without AO has been demonstrated [36,37], as well as with WFS-based AO methods [7]. However, it can be difficult to accurately measure the aberrations from a mouse eye without a high degree of system complexity, whereas SAO has the ability to perform depth-specific aberration correction at the cost of algorithmic execution time and the potential for errors due to sample motion [22]. This is important since high-resolution GFP imaging with NIR light could be used to investigate the visual response of RGCs with calcium indicators, such as GCaMP [7,36,38]. While the single photon excitation at 488 nm would provide a higher SNR, the NIR light used for TPEF is much less likely to activate the visual system. In this work, we used 9 mW of laser power at 910 nm to image the GFP labelled RGCs. It may be possible to measure a calcium response in the RGC by only imaging soma [37]. This could be performed with a significant reduction in the laser power, which may be similar or less than the 2.5 mW of laser power at 940 nm that was required for imaging the YFP labelled cells.

For TPEF, SAO is well-suited for good aberration correction performance due to the nonlinear relationship between the signal and the spot size [11]. Hence, the TPEF signal strength is significantly degraded in the presence of aberrations. The overall optimization convergence speed and performance could be improved by using a combination of aberration correction with the OCT signal, increasing the TPEF signal enough that it could be used for a second iteration of the SAO process for a more precise correction. Furthermore, even in the cases where there are poor structural features in the OCT at the location of the fluorophore, the SAO could potentially be improved with low-order aberrations using the OCT images before further optimization using the TPEF. Similarly, at a large imaging FOV, a faster initial optimization could have been used for partial aberration correction before reducing the FOV to an area interest where the aberration correction would have better performance [22].

The images of the RPE in this report had strong differences for each strain and appear to be affected by the type of accumulated compounds, pigmentation, and age of the mouse. In order to visualize the cellular mosaic of the RPE, the TPEF signal from the features at the edges of the cells had to be greater than the background signal. This was the case for the for the albino B6 mice and the pigmented rpe65 mouse, where fluorescent compounds were visualized near the RPE cell membrane [8,9]. Palczewska *et al.* [1] has recently reported results for imaging RPE of albino rpe65 mice with laser powers down to 1 mW by averaging many frames, and using ultra short light pulses down to ~20 femtoseconds into the eye. Our results use similar methods to average many frames, but we could potentially visualize the RPE mosaic with similar power levels by imaging the albino rpe65 mouse and by pre-compensating for the group velocity dispersion through the optical components. However, we would still be limited by our source at 70 to 100 fs without sacrificing tunability with a broader spectral bandwidth laser. As shown

in this paper, the strain of mouse is important for visualizing the RPE mosaic at low power levels. However, the lack of pigment in albino mouse strains could reduce the performance of WFS-based aberration correction.

Reducing the average laser power on the retina is important not only for robust longitudinal animal studies, but also for potential applications in human imaging [2,39]. Although our laser power levels for these results are not safe for human eye imaging, mouse imaging can be used to further develop imaging techniques to enable TPEF at safe power levels. Recently, it has been demonstrated that averaging hundreds of OCT volumes can produce high-resolution retinal imaging of transparent features, including RGCs [40,41]. This so called 'super-averaging' could enable all 100–900 TPEF frames to be co-registered with the OCT, which could further reduce the TPEF signal requirements.

In conclusion, we have demonstrated that SAO and OCT can be used to achieve non-invasive cellular-resolution TPEF imaging from a variety of fluorophores in the retina. The increase in TPEF signal after aberration correction enables imaging to be performed with less laser power than without AO. Finally, if safe levels exposure levels are determined, the techniques shown here could be developed for human imaging.

Funding

Disclosures

YJ: Seymour Vision (I), MVS: Seymour Vision (I).

References

1. G. Palczewska, P. Stremplewski, S. Suh, N. Alexander, D. Salom, Z. Dong, D. Ruminski, E. H. Choi, A. E. Sears, T. S. Kern, M. Wojtkowski, and K. Palczewski, "Two-photon imaging of the mammalian retina with ultrafast pulsing laser," JCI insight **3**(17), 121555 (2018).
2. C. Schwarz, R. Sharma, W. S. Fischer, M. Chung, G. Palczewska, K. Palczewski, D. R. Williams, and J. J. Hunter, "Safety assessment in macaques of light exposures for functional two-photon ophthalmoscopy in humans," Biomed. Opt. Express **7**(12), 5148–5169 (2016).
3. S. Marcos, J. S. Werner, S. A. Burns, W. H. Merigan, P. Artal, D. A. Atchison, K. M. Hampson, R. Legras, L. Lundstrom, G. Yoon, J. Carroll, S. S. Choi, N. Doble, A. M. Dubis, A. Dubra, A. Elsner, R. Jonnal, D. T. Miller, M. Paques, H. E. Smithson, L. K. Young, Y. Zhang, M. Campbell, J. Hunter, A. Metha, G. Palczewska, J. Schallek, and L. C. Sincich, "Vision science and adaptive optics, the state of the field," Vision Res. **132**, 3–33 (2017).
4. L. L. Molday, D. Wahl, M. V. Sarunic, and R. S. Molday, "Localization and functional characterization of the p.Asn965Ser (N965S) ABCA4 variant in mice reveal pathogenic mechanisms underlying Stargardt macular degeneration," Hum. Mol. Genet. **27**(2), 295–306 (2018).
5. D. Merino and P. Loza-Alvarez, "Adaptive optics scanning laser ophthalmoscope imaging: technology update," Clin. Ophthalmol. **10**, 743–755 (2016).
6. G. Palczewska, Z. Dong, M. Golczak, J. J. Hunter, D. R. Williams, N. S. Alexander, and K. Palczewski, "Noninvasive two-photon microscopy imaging of mouse retina and retinal pigment epithelium through the pupil of the eye," Nat. Med. **20**(7), 785–789 (2014).
7. R. Sharma, L. Yin, Y. Geng, W. H. Merigan, G. Palczewska, K. Palczewski, D. R. Williams, and J. J. Hunter, "In vivo two-photon imaging of the mouse retina," Biomed. Opt. Express **4**(8), 1285–1293 (2013).
8. P. Stremplewski, K. Komar, K. Palczewski, M. Wojtkowski, and G. Palczewska, "Periscope for noninvasive two-photon imaging of murine retina in vivo," Biomed. Opt. Express **6**(9), 3352–3361 (2015).
9. Y. Imanishi, M. L. Batten, D. W. Piston, W. Baehr, and K. Palczewski, "Noninvasive two-photon imaging reveals retinyl ester storage structures in the eye," J. Cell Biol. **164**(3), 373–383 (2004).
10. F. Helmchen and W. Denk, "Deep tissue two-photon microscopy," Nat. Methods **2**(12), 932–940 (2005).
11. W. Denk, J. Strickler, and W. Webb, "Two-photon laser scanning fluorescence microscopy," Science **248**(4951), 73–76 (1990).
12. N. S. Alexander, G. Palczewska, P. Stremplewski, M. Wojtkowski, T. S. Kern, and K. Palczewski, "Image registration and averaging of low laser power two-photon fluorescence images of mouse retina," Biomed. Opt. Express **7**(7), 2671–2691 (2016).

13. M. Cua, D. J. Wahl, Y. Zhao, S. Lee, S. Bonora, R. J. Zawadzki, Y. Jian, and M. V. Sarunic, "Coherence-Gated Sensorless Adaptive Optics Multiphoton Retinal Imaging," Sci. Rep. **6**(1), 32223 (2016).

14. J. Porter, H. Queener, J. Lin, K. Thorn, and A. Awwal, *Adaptive Optics for Vision Science: Principles, Practices, Design and Applications* (Wiley, 2006).

15. J. Schallek, Y. Geng, H. Nguyen, and D. R. Williams, "Morphology and topography of retinal pericytes in the living mouse retina using in vivo adaptive optics imaging and ex vivo characterization," Invest. Ophthalmol. Visual Sci. **54**(13), 8237–8250 (2013).

16. Y. Geng, A. Dubra, L. Yin, W. H. Merigan, R. Sharma, R. T. Libby, and D. R. Williams, "Adaptive optics retinal imaging in the living mouse eye," Biomed. Opt. Express **3**(4), 715–734 (2012).

17. Y. Geng, L. A. Schery, R. Sharma, A. Dubra, K. Ahmad, R. T. Libby, and D. R. Williams, "Optical properties of the mouse eye," Biomed. Opt. Express **2**(4), 717–738 (2011).

18. W. Drexler and J. G. Fujimoto, *Optical Coherence Tomography: Technology and Applications*, 2nd ed. (Springer, 2015).

19. R. H. Webb, "Confocal optical microscopy," Rep. Prog. Phys. **59**(3), 427–471 (1996).

20. Y. Jian, K. Wong, and M. V. Sarunic, "Graphics processing unit accelerated optical coherence tomography processing at megahertz axial scan rate and high resolution video rate volumetric rendering," J. Biomed. Opt. **18**(2), 026002 (2013).

21. D. J. Wahl, R. Ng, M. J. Ju, Y. Jian, and M. V. Sarunic, "Sensorless adaptive optics multimodal en-face small animal retinal imaging," Biomed. Opt. Express **10**(1), 252–267 (2019).

22. D. J. Wahl, P. Zhang, J. Mocci, M. Quintavalla, R. Muradore, Y. Jian, S. Bonora, M. V. Sarunic, and R. J. Zawadzki, "Adaptive optics in the mouse eye: wavefront sensing based vs. image-guided aberration correction," Biomed. Opt. Express **10**(9), 4757–4774 (2019).

23. P. Zhang, J. Mocci, D. J. Wahl, R. K. Meleppat, S. K. Manna, M. Quintavalla, R. Muradore, M. V. Sarunic, S. Bonora, E. N. Pugh, and R. J. Zawadzki, "Effect of a contact lens on mouse retinal in vivo imaging: Effective focal length changes and monochromatic aberrations," Exp. Eye Res. **172**, 86–93 (2018).

24. A. Myronenko and X. Song, "Intensity-based image registration by minimizing residual complexity," IEEE Trans. Med. Imaging **29**(11), 1882–1891 (2010).

25. M. Heisler, S. Lee, Z. Mammo, Y. Jian, M. Ju, A. Merkur, E. Navajas, C. Balaratnasingam, M. F. Beg, and M. V. Sarunic, "Strip-based registration of serially acquired optical coherence tomography angiography," J. Biomed. Opt. **22**(3), 036007 (2017).

26. D. C. Adler, T. H. Ko, and J. G. Fujimoto, "Speckle reduction in optical coherence tomography images by use of a spatially adaptive wavelet filter," Opt. Lett. **29**(24), 2878–2880 (2004).

27. M. Salas, M. Augustin, L. Ginner, A. Kumar, B. Baumann, R. Leitgeb, W. Drexler, S. Prager, J. Hafner, U. Schmidt-Erfurth, and M. Pircher, "Visualization of micro-capillaries using optical coherence tomography angiography with and without adaptive optics," Biomed. Opt. Express **8**(1), 207–222 (2017).

28. M. T. Bernucci, C. W. Merkle, and V. J. Srinivasan, "Investigation of artifacts in retinal and choroidal OCT angiography with a contrast agent," Biomed. Opt. Express **9**(3), 1020–1040 (2018).

29. A. Guevara-Torres, D. R. Williams, and J. B. Schallek, "Imaging translucent cell bodies in the living mouse retina without contrast agents," Biomed. Opt. Express **6**(6), 2106–2119 (2015).

30. J. I. W. Morgan, J. J. Hunter, B. Masella, R. Wolfe, D. C. Gray, W. H. Merigan, F. C. Delori, and D. R. Williams, "Light-Induced Retinal Changes Observed with High-Resolution Autofluorescence Imaging of the Retinal Pigment Epithelium," Invest. Ophthalmol. Visual Sci. **49**(8), 3715–3729 (2008).

31. W. T. Ham, H. A. Mueller, J. J. Ruffolo, and A. M. Clarke, "Sensitivity of the retina to radiation damage as a function of wavelength," Photochem. Photobiol. **29**(4), 735–743 (1979).

32. G. Palczewska, T. Maeda, Y. Imanishi, W. Sun, Y. Chen, D. R. Williams, D. W. Piston, A. Maeda, and K. Palczewski, "Noninvasive multiphoton fluorescence microscopy resolves retinol and retinal condensation products in mouse eyes," Nat. Med. **16**(12), 1444–1449 (2010).

33. S. He, C. Ye, Q. Sun, C. K. S. Leung, and J. Y. Qu, "Label-free nonlinear optical imaging of mouse retina," Biomed. Opt. Express **6**(3), 1055–1066 (2015).

34. D. J. Wahl, Y. Jian, S. Bonora, R. J. Zawadzki, and M. V. Sarunic, "Wavefront sensorless adaptive optics fluorescence biomicroscope for in vivo retinal imaging in mice," Biomed. Opt. Express **7**(1), 1–12 (2016).

35. Y. Jian, J. Xu, M. A. Gradowski, S. Bonora, R. J. Zawadzki, and M. V. Sarunic, "Wavefront sensorless adaptive optics optical coherence tomography for in vivo retinal imaging in mice," Biomed. Opt. Express **5**(2), 547–559 (2014).

36. T. Kamali, J. Fischer, S. Farrell, W. H. Baldridge, G. Zinser, and B. C. Chauhan, "Simultaneous in vivo confocal reflectance and two-photon retinal ganglion cell imaging based on a hollow core fiber platform," J. Biomed. Opt. **23**(09), 1 (2018).

37. A. S. Bar-Noam, N. Farah, and S. Shoham, "Correction-free remotely scanned two-photon in vivo mouse retinal imaging," Light: Sci. Appl. **5**(1), e16007 (2016).

38. L. Yin, Y. Geng, F. Osakada, R. Sharma, A. H. Cetin, E. M. Callaway, D. R. Williams, and W. H. Merigan, "Imaging light responses of retinal ganglion cells in the living mouse eye," J. Neurophysiol. **109**(9), 2415–2421 (2013).

39. C. Schwarz, R. Sharma, S. K. Cheong, M. Keller, D. R. Williams, and J. J. Hunter, "Selective S Cone Damage and Retinal Remodeling Following Intense Ultrashort Pulse Laser Exposures in the Near-Infrared," Invest. Ophthalmol. Visual Sci. **59**(15), 5973–5984 (2018).

40. Z. Liu, K. Kurokawa, F. Zhang, J. J. Lee, and D. T. Miller, "Imaging and quantifying ganglion cells and other transparent neurons in the living human retina," Proc. Natl. Acad. Sci. U. S. A. **114**(48), 12803–12808 (2017).
41. Z. Liu, J. Tam, O. Saeedi, and D. X. Hammer, "Trans-retinal cellular imaging with multimodal adaptive optics," Biomed. Opt. Express **9**(9), 4246–4262 (2018).